

# Parsec-scale morphology and spectral index distribution in faint high frequency peakers

M. Orienti<sup>1,2\*</sup>, D. Dallacasa<sup>1,2</sup>

<sup>1</sup>*Dipartimento di Astronomia, Università di Bologna, via Ranzani 1, I-40127, Bologna, Italy*

<sup>2</sup>*INAF - Istituto di Radioastronomia, Via P. Gobetti 101, I-40129 Bologna, Italy*

Received 6 February 2022; accepted ?

## ABSTRACT

We investigate the parsec-scale structure of 17 high frequency peaking radio sources from the faint HFP sample. VLBA observations were carried out at two adjacent frequencies, 8.4 and 15.3 GHz, both in the optically-thin part of the spectrum, to obtain the spectral index information. We found that 64% of the sources are resolved into subcomponents, while 36% are unresolved even at the highest frequency. Among the resolved sources, 7 have a morphology and a spectral index distribution typical of young radio sources, while in other 4 sources, all optically associated with quasars, the radio properties resemble those of the blazar population. The equipartition magnetic field of the single components are a few tens milliGauss, similar to the values found in the hotspots of young sources with larger sizes. Such high magnetic fields cause severe radiative losses, precluding the formation of extended lobe structures emitting at centimeter wavelengths. The magnetic fields derived in the various components of individual source are usually very different, indicating a non self-similar source evolution, at least during the very first stages of the source growth.

**Key words:** galaxies: active - radio continuum: general - radiation mechanisms: non-thermal

## 1 INTRODUCTION

Young radio sources can provide information on the birth and evolution of the radio emission originating in the central region of an active galactic nucleus (AGN). Powerful radio emission  $L_{1.4\text{GHz}} > 10^{24.5} \text{ W Hz}^{-1}$  is found only in a small fraction ( $\sim 10\%$ ) of the AGN population. The population of extragalactic radio sources is divided into several sub-classes each representing a different stage in the individual source life. In the evolutionary framework, the age of a radio source is directly related to its linear size (e.g. Fanti et al. 1995; Snellen et al. 2000). In this context, the empirical anticorrelation found by O’Dea & Baum (1997) between the intrinsic linear sizes,  $LS$ , and the spectral peak frequency  $\nu_p$  indicates an evolutionary path linking the different evolutionary stages: high frequency peakers (HFP,  $\nu_p > 5 \text{ GHz}$  and  $LS \ll 100 \text{ pc}$ ), will evolve into gigahertz-peaked spectrum (GPS,  $\nu_p \sim 1 \text{ GHz}$  and  $LS \leq 1 \text{ kpc}$ ), and then into compact steep-spectrum (CSS,  $\nu_p \sim 100 \text{ MHz}$  and  $LS \leq 15 \text{ kpc}$ ) objects, which are the progenitors of the classical Fanaroff-Riley I/II radio galaxies (FRI/FRII,  $LS$  up to a few Mpc, Fanaroff & Riley 1974). The genuine youth of CSS/GPS sources was proved by the

determination of both the kinematic (Owsianik & Conway 1998; Owsianik et al. 1998; Taylor et al. 2000; Tschager et al. 2000; Polatidis & Conway 2003; Orienti & Dallacasa 2010) and radiative (Murgia 2003; Orienti et al. 2007a, 2004) ages of a dozen of the most compact objects ( $LS \leq 100 \text{ pc}$ ), which turned out to be  $10^3$ - $10^4$  years.

With their typical linear sizes up to a few tens of parsecs, the sub-class of HFP should represent the very first stage in the radio source evolution, with ages of a few hundred years. Their radio properties have been derived by means of a detailed analysis of the flux density variability (Tinti et al. 2005; Orienti et al. 2007b), pc-scale morphology (Orienti et al. 2006) and polarization properties (Orienti & Dallacasa 2008a) of the sources from the “bright” HFP sample (Dallacasa et al. 2000). From these studies it became clear that the class of HFPs is made of two different populations. One consists of genuinely young radio sources: they are non-variable, with a double/triple structure resembling a scaled-down version of the classical FRIIs, whose radio emission, unpolarized, is dominated by hotspots/lobes. The other population is made of blazar sources, characterized by high level of variability, pc-scale core-jet structure and with significant polarized emission. Although blazars usually display a flat radio spectrum,

\* E-mail: orienti@ira.inaf.it

they may show a convex peaked spectrum during particular phases of their variability, i.e. when a self-absorbed knot in the jet dominates the radio emission. In the case of the bright HFP sample, almost 60% of the objects have blazar-like properties.

A high percentage of blazar objects in samples of high-frequency peaking objects was found by Tornainen et al. (2005), Bolton et al. (2006), Tornainen et al. (2007), and Hancock (2009) by monitoring the flux density variability of several HFP samples. However, among the HFP/GPS sources optically associated with a galaxy the percentage of genuinely young radio sources is larger than in objects hosted in quasars (e.g. Hancock et al. 2010; Stanghellini et al. 2005; Tinti et al. 2005), indicating that projection and boosting effects play a role in selecting objects in a high-activity state.

To investigate and compare the physical characteristics of HFPs spanning a broader luminosity range ( $L_{5\text{GHz}} \sim 10^{24}$  -  $10^{28}$  W/Hz) we performed analysis of the “faint” HFP sample (Stanghellini et al. 2009). Flux density and spectral variability studies of the sources in this sample were performed by means of multi-epoch VLA observations carried out at various frequencies simultaneously (Orienti et al. 2010). From this analysis it turned out that 42% of the sources are non-variable, while 21% are highly variable with their radio spectrum becoming flat at least in one observing epoch, as typical of the blazar population. The remaining sources maintain the convex peaked spectrum, but with some flux density variability. However, 37% of them possess a variability that can be explained in terms of a very young radio source undergoing (adiabatic) expansion, suggesting that a fraction of variable sources may still be genuinely young objects.

In this paper we continue the analysis of the radio properties of the sources from the “faint” HFP sample by means of VLBA observations at 8.4 and 15.3 GHz. Among the 61 sources of the sample we observed the 17 sources whose spectral peak occurred at a frequency below 8.4 GHz. The availability of two observing frequencies in the optically-thin part of the spectrum allows us to derive the spectral index distribution across the source structure to classify the nature of each sub-component and thus of each source. In the classical picture, young radio sources are characterized by a two-sided structure dominated by lobes/hotspots, like the population of compact-symmetric objects (CSO). On the other hand, one-sided flat-spectrum core-jet structure is typical of boosted sources.

The layout of the paper is the following: Section 2 describes the VLBA observations and the data reduction; Section 3 provides information on the radio morphology and spectral index distribution for each source; a concise discussion and a brief summary are reported in Sections 4 and 5.

Throughout this paper we assume  $H_0 = 71 \text{ km s}^{-1} \text{ Mpc}^{-1}$ ,  $\Omega_M = 0.27$ ,  $\Omega_\Lambda = 0.73$ , in a flat Universe. The spectral index  $\alpha$  is defined as  $S(\nu) \propto \nu^{-\alpha}$ .

**Table 1.** Log of the VLBA observations

Code	Obs. date	Obs. time	Info
BD147A	15 Feb 2010	5.5 hr	No SC
BD147B	20 Feb 2010	7.0 hr	-
BD147C	04 Mar 2010	7.0 hr	-
BD147D	01 Mar 2010	4.5 hr	No SC

## 2 VLBA OBSERVATIONS AND DATA REDUCTION

We performed VLBA observations at 8.4 and 15.3 GHz of 17 sources from the faint HFP sample (Stanghellini et al. 2009). The targets were chosen on the basis of their spectral peak occurring at a frequency below 8.4 GHz, in order to study the optically-thin part of the spectrum. VLBA observations were carried out between February and March 2010 (Table 1), in single polarization with an aggregate bit-rate of 256 Mbps. The correlation was performed at the VLBA correlator in Socorro.

Each source was observed for about 30 min at 8.4 GHz and 1 hr at 15.3 GHz, spread into 7 to 9 short scans of about 3 minutes each, switching between frequencies and sources in order to improve the coverage of the  $uv$ -plane. The strong sources DA 193, and 4C 39.25 were used as fringe finders and bandpass calibrators. Phase referencing was performed for the 8 targets fainter than 35 mJy. Due to their proximity to the phase calibrators used for other targets, we could observe three additional sources (J0804+5431, J1319+4851, and J1436+4820) in phase-referencing mode in order to determine their accurate position.

The data handling was carried out by means of the NRAO AIPS package. A priori amplitude calibration was derived using measurements of the system temperature and the antenna gains. The errors on the absolute flux density scale were estimated by comparing the data of either DA 193 or 4C 39.25 with the values reported in the VLA/VLBA database. They resulted to be within 10% ( $\sigma_c$ ).

Final images were produced after a number of phase self-calibration iterations. Amplitude self-calibration was applied at the end of the process only for the brightest sources, in order to remove residual systematic errors, and using a solution interval longer than the scan-length. The flux densities of our targets are generally in agreement with those measured with the VLA. The rms noise level on the image plane is between 0.05 and 0.25 mJy/beam. Therefore, the main uncertainty in the flux densities generally comes from the amplitude calibration errors.

## 3 RESULTS

Of the 17 sources with VLBA observations, 6 are resolved at both frequencies, while 5 sources are resolved at the higher frequency only. The remaining 6 sources are unresolved even with the high resolution provided by the 15.3 GHz VLBA observations (FWHM  $\sim 1$  mas).

Throughout the paper we consider “marginally resolved” (MR) those sources whose largest angular size (LAS) detected is between 0.5 and 1 times the beam size at 15.3

GHz, and we term "Unresolved" (Un) all the sources whose LAS is smaller than half the beam size at both frequencies. The total flux density of each source is reported in Table 2 and was measured by means of TVSTAT which performs an aperture integration over a selected region on the image plane. For the resolved sources we also derived the flux density and the deconvolved angular size of each source component by means of the AIPS task JMFIT which performs a Gaussian fit to the source components on the image plane. The formal uncertainty on the deconvolved angular size obtained from the fit is  $\leq 0.1$  mas. As expected, the sum of the flux density from each component agrees with the total flux density measured on the whole source structure. Source components are referred to as North (N), South (S), East (E), West (W), and Central (C). Observational parameters of the source components are reported in Table 3.

The uncertainty on the flux density arises from both the calibration error  $\sigma_c$  (see Section 2), and the measurement error  $\sigma_m$ . The latter represents the off-source noise level, rms, measured on the image plane and it is related to the source size  $\theta_{\text{obs}}$  normalized by the beam size  $\theta_{\text{beam}}$  as  $\sigma_m = \text{rms} \times (\theta_{\text{obs}}/\theta_{\text{beam}})^{1/2}$ . The flux density errors  $\sigma_S$  reported in Tables 2 and 3 take into consideration both uncertainties, and they correspond to  $\sigma_S = \sqrt{\sigma_c^2 + \sigma_m^2}$ . Errors on the spectral index  $\alpha_{8.4}^{15}$  have been computed assuming the error propagation theory. In general the uncertainty on the overall component spectral index is  $\sim 0.1$ - $0.2$  in the most compact and brightest components, while it becomes larger in the weakest ones (Tables 2 and 3).

For those sources observed with the phase-referencing technique we could derive the accurate absolute position, reported in Table 4, not available previously. In fact, the majority of the targets lack previous mas-resolution observations, and the coordinate information was obtained from the FIRST survey (Becker et al. 1995). In earlier multifrequency VLA observations, the snapshots were very short, and for most sources the secondary calibrator was often too far away to provide accurate information on the source position. The uncertainty on the source position derived from these VLBA data is about 0.5 mas. Such uncertainties have been estimated for the sources observed in phase referencing at both frequencies, by comparing the positions derived at both 8.4 and 15.3 GHz.

### 3.1 Source images

Full-resolution images of the 6 sources with resolved structure at both frequencies are presented in Fig. 1. In Fig. 2 we present the full-resolution images at 15.3 GHz of the sources which are marginally resolved at this frequency only.

For the sources with resolved morphology at both frequencies, to produce spectral index images in addition to the full-resolution images, we produced also low-resolution images at both frequencies using the same  $uv$ -range between 11 M $\lambda$  and 240 M $\lambda$ . Furthermore, the images have been produced at both frequencies with the same image sampling, natural grid weighting and, in the case of the 15.3 GHz, by forcing the beam major and minor axes, and

position angle to be equal to those of the 8.4-GHz image. The spectral index images were produced by combining the low-resolution images at both frequencies by means of the AIPS task COMB. Blanking was done clipping the pixels of the input images with values below three times the rms measured on the off-source image plane at each frequency. Image registration was performed by comparing the position of the source components and applying an image shift using the AIPS task LGEOM, when necessary. The greyscale spectral index images superimposed on the 15.3 GHz contours are presented in Fig. 3. Despite the particular care used to produce these images, some gradients in the direction transverse to the source axis are present in a few sources, likely due to the poor  $uv$ -coverage of these short observations. This is particularly critical in the case of J0943+5113 where the artificial gradients do not allow us to reliably measure the spectral index across the Western component.

### 3.2 Notes on individual sources

In this section we discuss in detail the observational properties of the sources with resolved morphology. In general the spectral index distribution is uniform across the source components, and the value computed by means of the total flux density of the whole component measured from the full-resolution images at 8.4 and 15.3 GHz (Table 3), agrees with the one directly measured on the spectral index image (Fig. 3). The use of the total flux density in computing the spectral index may cause an artificial steepening due to the absence of the shortest spacing at the higher frequency. Since our targets do not possess diffuse emission, the estimated spectral indices should not be severely affected by the different  $uv$ -coverages. However, there are a few source components, remarked in the following discussion, where a non-artificial spectral index gradient is present. Following Orienti et al. (2006), we consider CSO candidates (labelled CSO? in Table 2) those sources with a spectral index between 8.4 and 15.3 GHz  $> 0.5$  (Table 2), and a double/triple pc-scale structure whose components have a steep spectral index (Table 3). When the central core is present, we classify the source as a genuine CSO (labelled CSO in Table 2). On the other hand, we classify blazar objects (labelled BL in Table 2) those sources with a spectral index  $< 0.5$  between 8.4 and 15.3 GHz (Table 2) and/or with a Core-Jet-like morphology, i.e. one-sided structure dominated by a compact flat-spectrum component (containing the core) from which a steep-spectrum jet-like component emerges. When the source is unresolved and both the spectral index information and the variability behaviour is unclear, we do not attempt any classification (the source is labelled "?" in Table 2.)

#### 3.2.1 Sources resolved at both 8.4 and 15.3 GHz

Here we discuss the sources marked as "Resolved" in Table 2. The images of these sources are shown in Fig. 1: left and right panels present the VLBA image at 8.4 and 15.3 GHz respectively. The spectral indices reported in the following

**Table 2.** The VLBA sample. Column 1: source name (J2000); Col. 2: optical identification; Q=quasar, G=galaxy, EF=empty field; Col. 3: redshift; a “p” indicates a photometric redshift from Orienti et al. (2010); Cols. 4, 5: VLA flux density at 8.4 and 15.3 GHz respectively, from Stanghellini et al. (2009); Cols. 6, 7: VLBA flux density at 8.4 and 15.3 GHz, respectively; Col. 8: luminosity at 1.4 GHz, computed using the flux density at 1.4 GHz reported in Stanghellini et al. (2009); Col. 9: VLBA spectral index computed between 8.4 and 15.3 GHz; Col. 10: VLBA structure: Res=resolved; MR=marginally resolved; Un=unresolved; Col. 11: source classification: CSO= genuine CSO; CSO?=CSO candidate; BL=blazar-like object; ?=not enough information to reliably classify the source nature.

Source	ID	z	S <sub>8.4</sub> <sup>VLA</sup> mJy	S <sub>15.3</sub> <sup>VLA</sup> mJy	S <sub>8.4</sub> <sup>VLBA</sup> mJy	S <sub>15.3</sub> <sup>VLBA</sup> mJy	L <sub>1.4GHz</sub> W/Hz	α <sub>8.4</sub> <sup>15</sup>	Morph	Class
(1)	(2)	(3)	(4)	(5)	(6)	(7)	(8)	(9)	(10)	(11)
J0736+4744	Q	-	47	30	45±5	33±3	26.86	0.5±0.2	MR	?
J0804+5431	G	0.22p	67	49	53±5	41±4	25.48	0.4±0.2	MR	?
J0819+3823	Q	-	91	44	86±8	46±5	27.11	1.1±0.2	Un	?
J0905+3742	EF	-	68	39	65±6	40±4	26.99	0.8±0.2	Res	CSO?
J0943+5113	G	0.42p	64	26	59±6	23±2	26.10	1.4±0.2	Res	CSO?
J0951+3451	G	0.29p	55	38	55±6	52±5	25.66	0.1±0.2	Res	CSO
J0955+3335	Q	2.491	105	70	52±5	40±4	28.09	0.4±0.2	Un	BL
J1002+5701	EF	-	71	20	53±5	13±2	27.02	2.3±0.3	MR	CSO?
J1008+2533	Q	1.960	96	74	88±9	128±13	27.83	-0.6±0.2	Res	BL
J1107+3421	EF	-	51	32	32±3	20±2	26.87	1.0±0.2	Res	CSO?
J1135+3624	EF	-	41	22	41±4	18±2	26.78	1.4±0.2	Res	CSO?
J1241+3844	Q	-	21	17	15±2	16±2	26.49	0.1±0.3	Un	BL
J1309+4047	Q	2.910	95	59	85±9	37±4	28.22	1.4±0.3	MR	CSO?
J1319+4851	Q	-	37	27	33±3	37±4	26.73	-0.2±0.2	MR	BL
J1420+2704	Q	-	51	37	61±6	44±4	26.88	0.5±0.2	Un	?
J1436+4820	EF	-	62	40	49±5	29±3	26.95	0.9±0.2	Un	?
J1613+4223	Q	-	122	44	100±10	31±3	27.25	2.0±0.2	Un	?

**Table 3.** Parameters of the components of resolved sources. Column 1: source name; Col. 2: source component labelled as in Fig. 1; Cols. 3, 4: flux density at 8.4 and 15.3 GHz, respectively; Cols. 5, 6: deconvolved major and minor axis, respectively; Col. 7: position angle of the major axis; Col. 8: spectral index between 8.4 and 15.3 GHz computed considering the total flux density of the whole component measured from the full-resolution images at 8.4 and 15.3 GHz (see Section 3.2); Cols. 9 and 10: angular and linear separation from the brightest component; Col. 11: equipartition magnetic field (see Section 4.3). When neither a spectroscopic nor photometric redshift is available, we compute the linear separation assuming  $z = 1.0$ .

Source	Comp	S <sub>8.4</sub> mJy	S <sub>15.3</sub> mJy	θ <sub>max</sub> mas	θ <sub>min</sub> mas	PA	α	Sep. mas	Lin. pc	H <sub>eq</sub> mG
(1)	(2)	(3)	(4)	(5)	(6)	(7)	(8)	(9)	(10)	(11)
J0905+3742	E	51±5	30±3	0.722 <sup>+0.005</sup> <sub>-0.005</sub>	-	133±1	0.9±0.2			>60
	W	14±2	10±2	1.692 <sup>+0.035</sup> <sub>-0.029</sub>	0.790 <sup>+0.063</sup> <sub>-0.068</sub>	74±2	0.6±0.4	1.7±0.1	13.7±0.8	10
J0943+5113	E	17±2	10±2	<0.4	<0.2	-	0.9±0.4			>27
	W	43±4	12±2	0.769±0.005	0.521 <sup>+0.119</sup> <sub>-0.169</sub>	73±20	2.1±0.3	3.9±0.2	21.5±1.1	13
J0951+3451	E	18±2	13±2	0.331 <sup>+0.022</sup> <sub>-0.021</sub>	<0.1	8±4	0.5±0.3	2.3±0.1	9.9±0.4	>40
	C	33±3	33±3	0.355 <sup>+0.004</sup> <sub>-0.003</sub>	0.203 <sup>+0.017</sup> <sub>-0.019</sub>	58±2	0.0±0.2			35
	W	4±1	2±1	1.452 <sup>+0.113</sup> <sub>-0.118</sub>	0.564 <sup>+0.086</sup> <sub>-0.111</sub>	-	1.1±0.9	2.5±0.2	10.8±0.9	7
J1008+2533	W	58±6	115±12	0.120±0.004	0.082±0.012	54±8	-1.1±0.2	1.0±0.1	8.5±0.8	210
	C	-	3±1	-	-	-	-			
	E	30±3	10±1	0.776±0.030	0.257 <sup>+0.074</sup> <sub>-0.105</sub>	106	1.8±0.2	1.6±0.1	13.6±0.8	41
J1107+3421	E	21±2	13±1	0.770±0.013	0.225 <sup>+0.016</sup> <sub>-0.019</sub>	7±1	0.8±0.2			>46
	W	11±1	6±1	0.323 <sup>+0.097</sup> <sub>-0.136</sub>	0.304 <sup>+0.106</sup> <sub>-0.141</sub>	130±40	1.0±0.3	1.2±0.2	9.6±1.6	12
J1135+3624	W	28±3	11±2	0.252±0.032	0.138 <sup>+0.134</sup> <sub>-0.029</sub>	-	1.5±0.3			60
	E	13±1	6±1	1.180 <sup>+0.150</sup> <sub>-0.161</sub>	0.886 <sup>+0.146</sup> <sub>-0.173</sub>	31±16	1.3±0.3	1.3±0.2	10.4±1.6	11

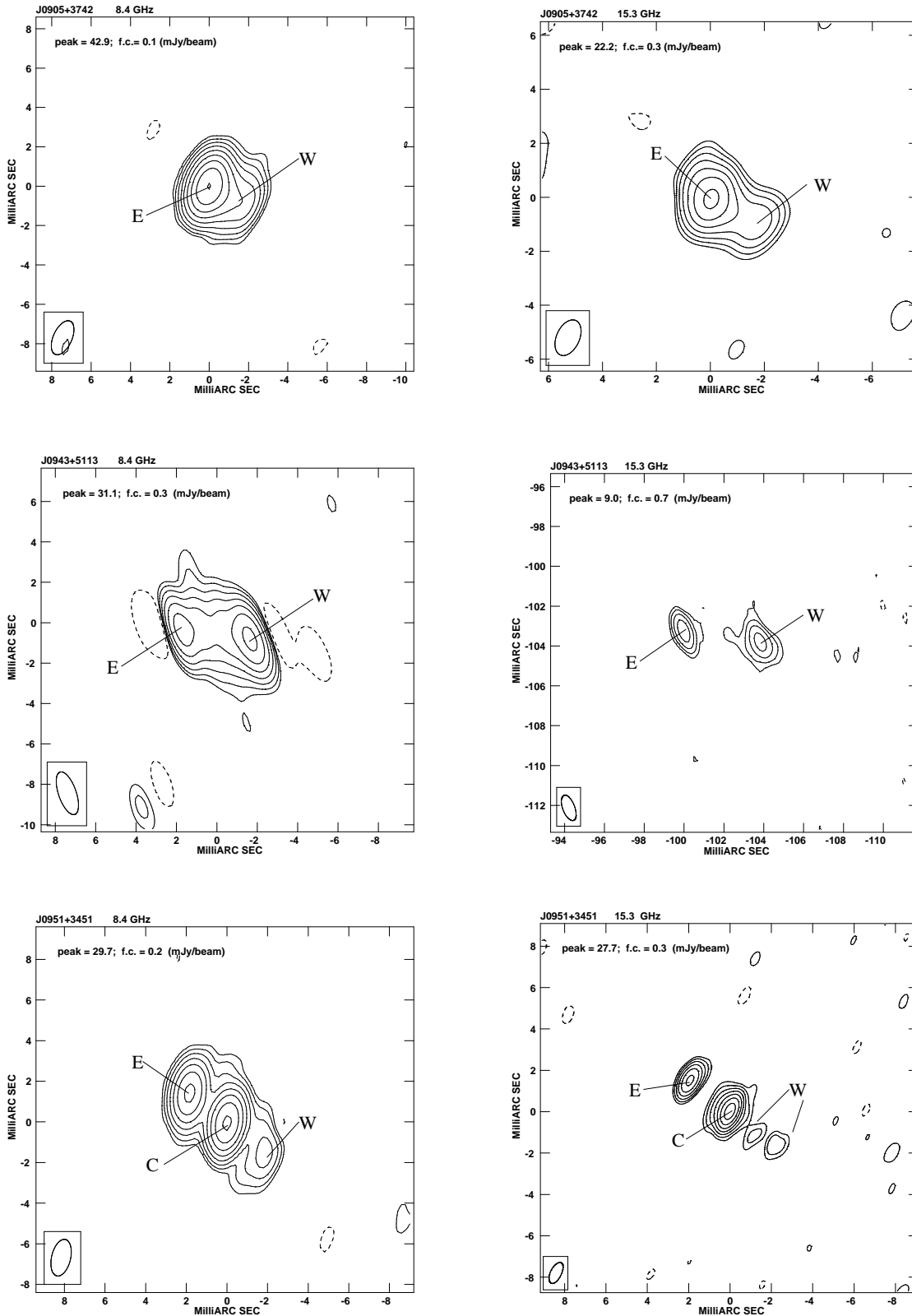


**Figure 1.** VLBA images at 8.4 (*left*) and 15.3 GHz (*right*) of the sources with a resolved structure at both frequencies. For each image we provide the observing frequency, peak flux density (mJy/beam), the first contour intensity which corresponds to three times the off-source noise level on the image plane. Contours increase by a factor of 2. The restoring beam is plotted on the bottom left corner. Positions are relative to those used in the correlator.

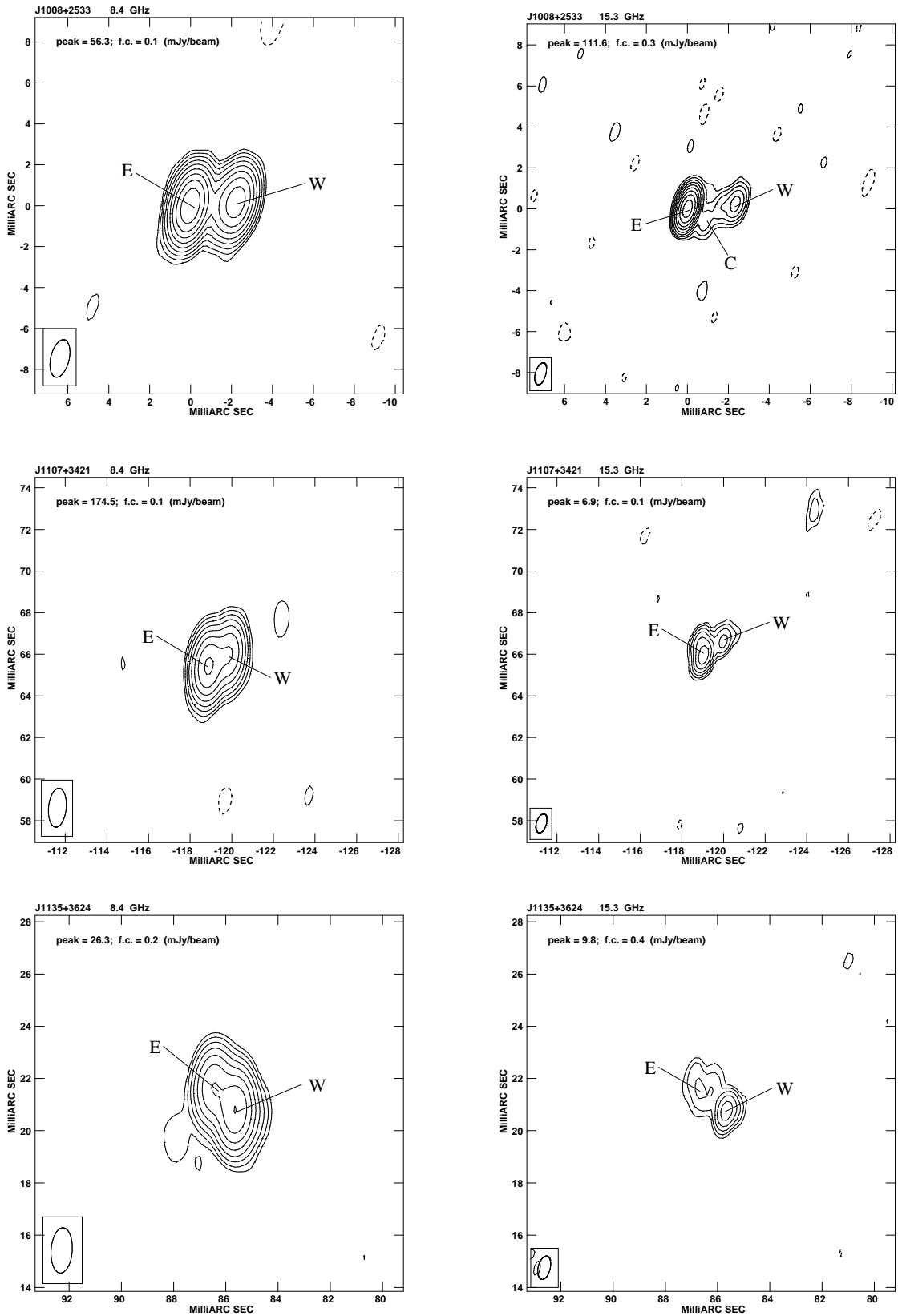
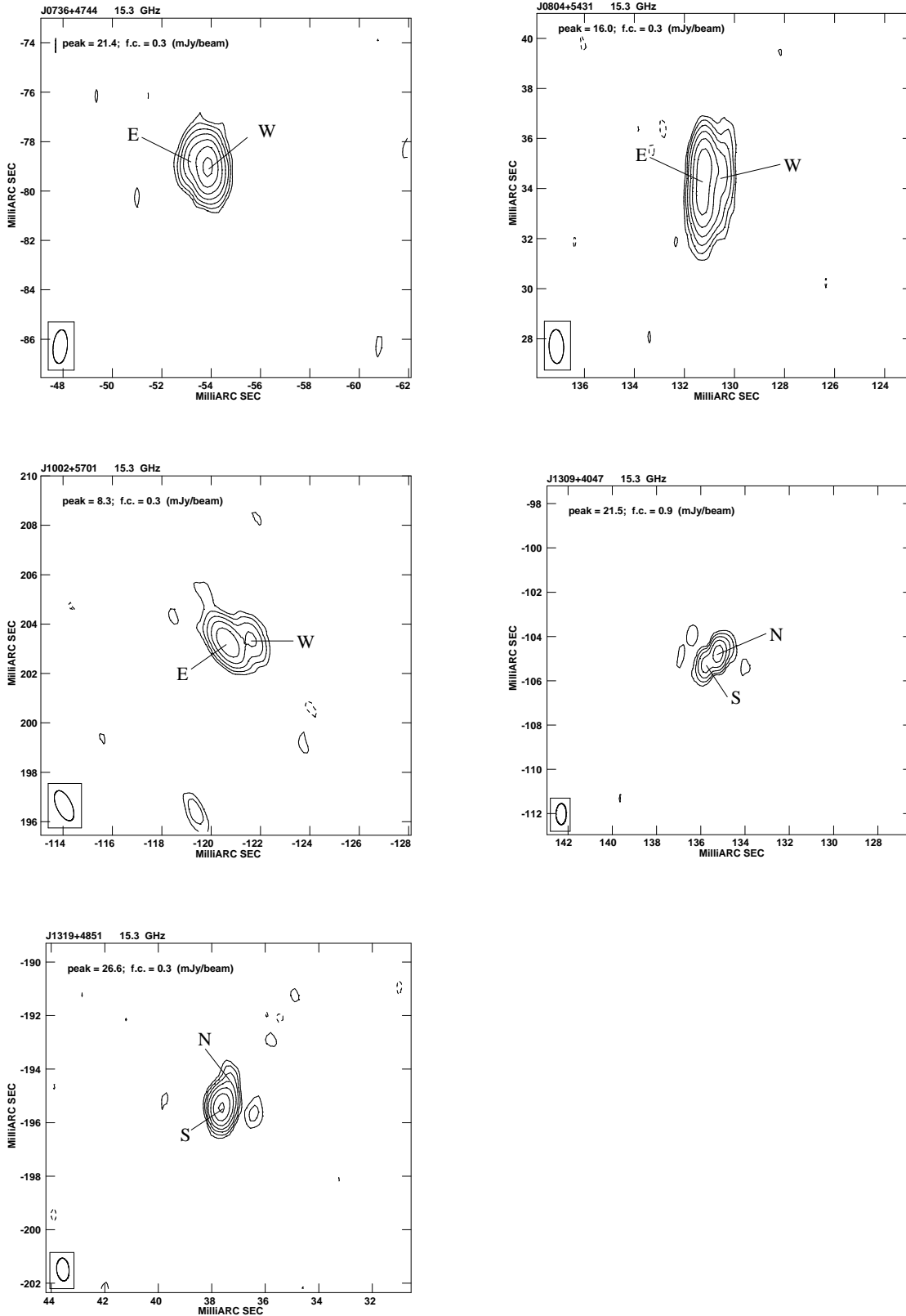
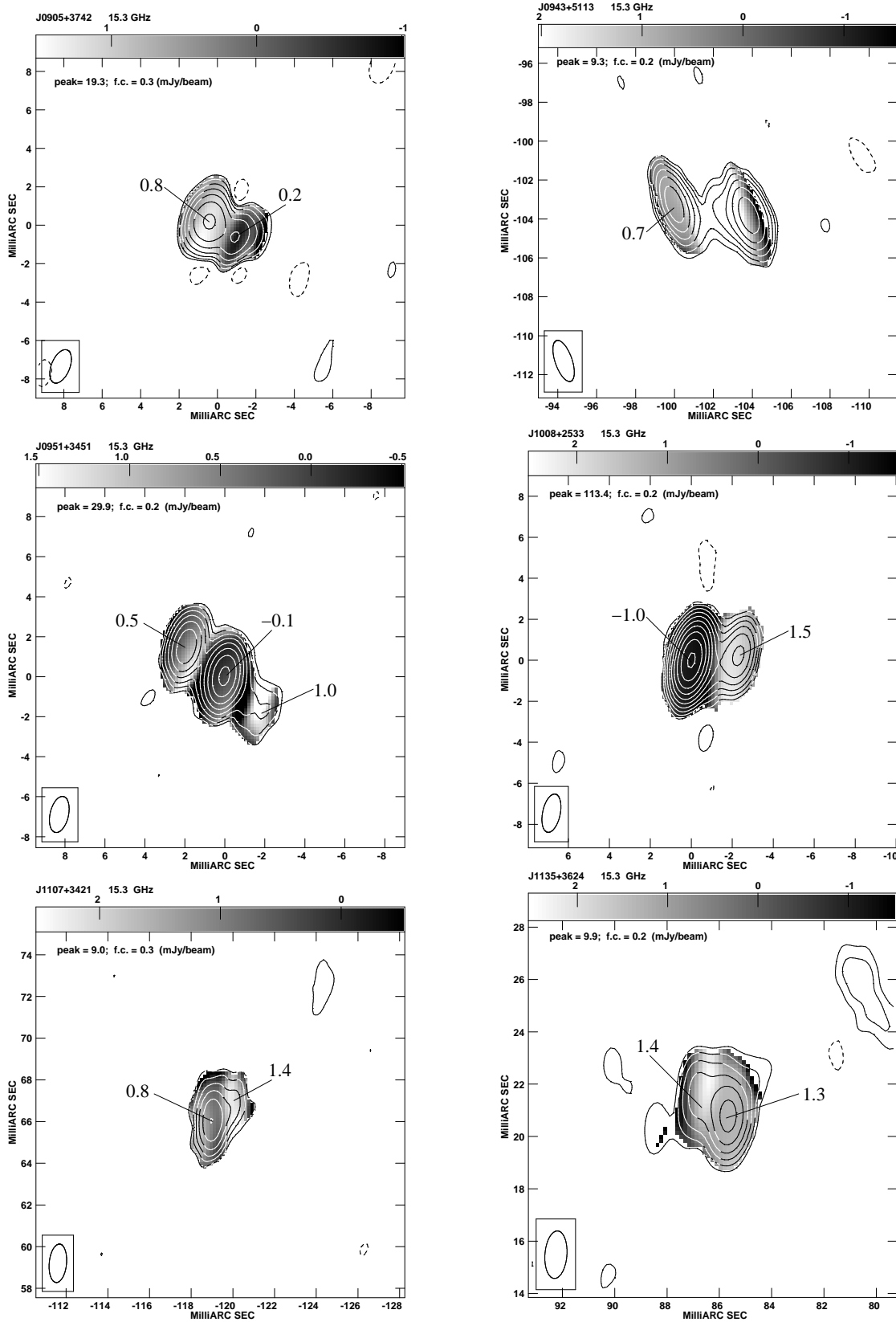


Figure 1. Continued.



**Figure 2.** VLBA images at 15.3 GHz of the sources with a marginally resolved structure. For each image we provide the observing frequency, peak flux density (mJy/beam), the first contour intensity which corresponds to three times the off-source noise level on the image plane. Contours increase by a factor of 2. The restoring beam is plotted on the bottom left corner. Positions are relative to those used in the correlator.



**Figure 3.** Greyscale spectral-index images between 8.4 and 15.3 GHz of the sources with a resolved structure at both frequencies, superimposed on the low-resolution 15.3-GHz contour image convolved with the 8.4-GHz beam. For each panel we provide the observing frequency, peak flux density (mJy/beam), and the first contour intensity which corresponds to three times the off-source noise level on the image plane. Contours increase by a factor of 2. The restoring beam is plotted on the bottom left corner. Positions are relative to those used in the correlator.



discussion are those from Table 3 and they were computed considering the total flux density of the whole component. In the case we consider the spectral index derived from the flux density peak on the spectral index images, we explicitly say that we are considering the local spectral index, and we make a reference to Fig. 3.

- J0905+3742: the radio structure of this source is characterized by two compact and asymmetric components separated by 1.7 mas and position angle of about  $-130^\circ$  (Fig. 1). The flux density ratio  $S_E/S_W$  is 3.6 and 3.0 at 8.4 and 15.3 GHz respectively. The eastern component has a steep spectrum with  $\alpha \sim 0.9$ . The spectral index distribution in the western component is more inhomogeneous, with an averaged spectral index  $\alpha \sim 0.6$ , that can reach locally  $\alpha \sim 0.2$  (Fig. 3). From its characteristics, we consider J0905+3742 a CSO candidate. The flux density obtained from our VLBA data is in good agreement with that derived from earlier VLA observations at both frequencies.

- J0943+5113: this source has an asymmetric double structure of 3.9 mas (21.5 pc at  $z=0.42$ ) in size and position angle of about  $85^\circ$  (Fig. 1). The flux density ratio  $S_W/S_E$  is 3.6 and 1.2 at 8.4 and 15.3 GHz respectively, indicating a different spectral index for the two components. Although the western component is the brighter, it has a very steep spectral index ( $\alpha = 2.1$ ), suggesting that relativistic particles undergo severe energy losses not balanced by acceleration processes. This value may be artificially steeper due to flux density losses at 15.3 GHz, but it agrees with the spectral index derived from the optically thin total spectral index ( $\alpha = 1.4$ , Orienti et al. 2007b), indicating that the integrated source spectrum is dominated by the western component. On the other hand, the spectrum of the eastern component is flatter, with a local spectral index  $\alpha \sim 0.7$  (Fig. 3). Diffuse emission connecting the main components is detected at 8.4 GHz, whereas at 15.3 GHz it is visible in the low-resolution image only (Fig. 3). On the basis of the morphological information, we classify J0943+5113 as a CSO candidate. The flux density obtained from our VLBA data is about 90% of that derived from VLA observations at both frequencies. This difference can be explained either by some degree of variability, or by some missing flux density not detected by the VLBA. No significant variability was found in earlier VLA observations (Orienti et al. 2010).

- J0951+3451: this source shows a highly asymmetric triple structure of 4.8 mas (20.7 pc at  $z=0.29$ ) in size and position angle of about  $45^\circ$  (Fig. 1). The central component has a flat spectrum ( $\alpha \sim 0$ ) and likely hosts the source core. The radio emission mainly comes from the central and the eastern components while the western component represents only 7% and 4% of the total flux density at 8.4 and 15.3 GHz respectively. The flux density ratio  $S_E/S_W$  is 4.5 and 6.5 at 8.4 and 15.3 GHz, respectively. With a spectral index  $\alpha \sim 0.5$ , component E is likely a hotspot. Component W has a steeper spectrum ( $\alpha \sim 1.1$ , Fig. 3), and at 15.3 GHz its structure is resolved into two aligned subcomponents. From its parsec-scale structure and the detection of the core, we classify J0951+3451 a genuine CSO. Furthermore, the flux density obtained from our VLBA data is in good agreement with that derived from VLA observations at

both frequencies. No significant variability was found in earlier VLA observations (Orienti et al. 2010).

- J1008+2533: at 15.3 GHz the source displays a core-jet structure with size of 2.6 mas (22.1 pc at  $z=1.96$ ) and position angle of about  $-70^\circ$ , while at 8.4 GHz it appears as a double with  $S_E/S_W \sim 2$  (Fig. 1). The eastern component has an inverted spectrum  $\alpha \sim -1.1$ , while the jet-like feature has a steep spectral index  $\alpha \sim 1.8$ . When imaged with the higher resolution of the 15.3-GHz data, an additional compact component, labelled C in Fig. 1, is clearly visible at about 1 mas (8.5 pc) from the core, and it may be a knot of the jet. These characteristics suggest that J1008+2533 is a blazar rather than a genuinely young object.

- J1107+3421: this radio source has an asymmetric double structure of 1.2 mas in size and position angle of about  $-50^\circ$  (Fig. 1). The flux density ratio  $S_E/S_W$  is 1.9 and 2.1 at 8.4 and 15.3 GHz, respectively. Component E has a spectral index  $\alpha \sim 0.8$ , while component W, which is also the fainter one, has a steeper spectrum. On the basis of these morphological properties we classify J1107+3421 a CSO candidate. However, the flux density obtained from our VLBA data is about 65% of that derived from earlier VLA observations at both frequencies. This difference can be explained either by some degree of variability, or by some flux density not detected by the VLBA. No significant variability was found in earlier VLA observations (Orienti et al. 2010).

- J1135+3624: this radio source shows an asymmetric double structure of 1.3 mas and position angle of about  $40^\circ$  (Fig. 1). The flux density ratio  $S_W/S_E$  is 2.1 and 1.8 at 8.4 and 15.3 GHz respectively. Component W is the brighter one and it has a compact structure at both the observing frequencies, while component E is resolved at 15.3 GHz. Both components have steep spectra, locally reaching a spectral index value of 1.3 and 1.5 for component W and E, respectively (Fig. 3). On the basis of these morphological properties we classify J1135+3624 a CSO candidate. The flux density obtained from our VLBA data is in good agreement with that derived from VLA observations at both frequencies. No significant variability was found in previous VLA observations (Orienti et al. 2010).

### 3.2.2 Sources resolved at 15.3 GHz only

Here we discuss the sources marked as ‘‘Marginally Resolved’’ in Table 2. For these sources only the VLBA image at 15.3 GHz is shown in Fig. 2, since in the 8.4-GHz image they appear point-like. For these sources the only value of the spectral index is that computed from the total flux density measured on the full-resolution images at 8.4 and 15.3 GHz. For this reason flux density and spectral index variations, with respect to those values reported in Orienti et al. (2010), are not independent.

- J0736+4744: this source is marginally resolved into two compact components separated by 0.8 mas in position angle of about  $70^\circ$  (Fig. 2). The spectral index computed considering the VLBA flux density integrated on the whole source is  $\alpha \sim 0.5$ , slightly flatter than the value derived from the

VLA data ( $\alpha \sim 0.8$  Orienti et al. 2010). The flux densities obtained from our VLBA data is in good agreement with that derived from VLA observations at both frequencies. However, the lack of a secure morphological classification does not allow us to reliably constrain the nature of this source.

- J0804+5431: this source is marginally resolved into two components separated by 0.9 mas (3.2 pc at  $z=0.22$ ) in position angle of about  $-60^\circ$  (Fig. 2). The spectral index computed considering the VLBA flux density integrated on the whole source is  $\alpha \sim 0.4$ , in agreement with the one derived from the VLA data (Orienti et al. 2010). The flux density obtained from our VLBA data is about 80% of that derived from VLA observations at both frequencies. This difference can be explained either by some degree of variability, or by some flux density not detected by the VLBA. No significant variability was found in earlier VLA observations (Orienti et al. 2010). However, the lack of a secure morphological classification does not allow us to reliably constrain the nature of this source.

- J1002+6701: this source is resolved into two components separated by 1.5 mas in position angle of about  $-70^\circ$  (Fig. 2). The spectral index computed considering the VLBA flux density integrated on the whole source is very steep ( $\alpha \sim 2.3$ ). Although such a steep value may be due to missing flux density at the higher frequency, it must be noted that the value derived from VLA data is also very steep ( $\alpha \sim 1.8$ , Orienti et al. 2010). On the basis of this steep spectral index we consider J1002+6701 a CSO candidate. However, the flux density obtained from our VLBA data is about 75% of that derived from VLA observations at both frequencies. This difference can be explained either by some degree of variability, or by some flux density not detected by the VLBA. No significant variability was found in earlier VLA observations (Orienti et al. 2010).

- J1309+4047: this source is resolved into two components separated by 0.8 mas (6.3 pc at  $z=2.91$ ) in position angle of about  $140^\circ$  (Fig. 2). The spectral index computed considering the VLBA flux density integrated on the whole source is steep ( $\alpha \sim 1.4$ ). Such a steep value may be due to missing flux density at the higher frequency. The spectral index derived from VLA data is  $\alpha \sim 0.9$  (Orienti et al. 2010). On the basis of this steep spectral index we still consider J1309+4047 a CSO candidate. However, the flux density obtained from our VLBA data is about 90% and 65% of that derived from VLA observations at 8.4 and 15.3 GHz, respectively. This difference can be explained either by some degree of variability, or by some flux density not detected by the VLBA. No significant variability was found in earlier VLA observations (Orienti et al. 2010).

- J1319+4851: this source is marginally resolved into two components separated by 0.6 mas in position angle of about  $30^\circ$  (Fig. 2). The spectral index computed considering the VLBA flux density integrated on the whole source is inverted ( $\alpha \sim -0.2$ ), while from previous VLA observations, between these frequencies the spectrum was already optically thin with  $\alpha \sim 0.5$  (Orienti et al. 2010). On the basis of these spectral characteristics we consider J1319+4851 a

blazar object rather than a genuine CSO. The flux density obtained from our VLBA data is about 85% of that derived from VLA observations at 8.4 GHz, while at 15.3 GHz the VLBA and VLA flux densities are in good agreement. No significant variability has been previously detected from the VLA monitoring campaign (Orienti et al. 2010).

## 4 DISCUSSION

Multifrequency observations with parsec-scale resolution are necessary to characterize the morphology of compact radio sources. The addition of the information on the spectral index distribution in the optically-thin part of the spectrum enables a suitable classification of each source component as hotspot, jet, core, or lobe, providing a crucial tool to determine whether the source is either genuinely young or a blazar. The optically-thin steep integrated spectral index guarantees that the most luminous components are likely hotspots rather than cores, at least at the two frequencies considered here. In most cases, the flux density measured in our VLBA images agrees with that detected by VLA observations a few years earlier. This means that the majority of the sources are not significantly variable, contrary to that expected in the case of blazars. A difference between VLBA and VLA detected flux densities may be related to some extended low-surface brightness emission due to the insufficient dynamic range of our observations.

### 4.1 The source morphology

From our VLBA observations we could resolve the source structure of 11 sources ( $\sim 65\%$ ) at least at 15.3 GHz. Among them, nine objects ( $\sim 82\%$ ) show a double structure (J0736+4744, J0804+5431, J0905+3742, J0943+5113, J1002+5751, J1107+3421, J1135+3624, J1309+4047, and J1319+4851), while two ( $\sim 18\%$ ) are resolved into three well-defined components (J0951+3451 and J1008+2533). For the six sources whose structure is resolved also in the 8.4-GHz data, we could classify the nature of each sub-component by means of the information on the spectral index. Compact components with spectral indices between 0.5 and 0.8, likely hotspots, are found in four sources (the eastern component of the sources J0905+3642, J0943+5113, J0951+3451, and J1107+3421). Despite its nearly flat spectral index ( $\alpha = 0.2$ ), we consider component W of J0905+3742 a very compact hotspot, rather than the true source core, with the spectral peak occurring at a frequency close to 8.4 GHz which causes an artificial flattening of the spectrum, as in the case of the very compact hotspots found in a few HFPs from the bright HFP sample (e.g. J1335+5844 and J1735+5049, Orienti et al. 2006).

The core component is unambiguously detected in two sources: the galaxy J0951+3451 and the quasar J1008+2533. In the former object the core is the central component, almost midway between the source hotspots/lobes. This source resembles the bright HFP quasar J0650+6001, where the asymmetric properties are well explained by Doppler boosting effects (Orienti & Dallacasa 2010). However, J0951+3451 is associated with a galaxy where projection effects should not play a relevant role, as also suggested by

the lack of both flux density and spectral variability in this object (Oriente et al. 2010). The different characteristics shown by the two external components might also be related to an inhomogeneous external medium surrounding the radio source. The interaction of one jet with a denser medium, like a cloud, may slow down the jet expansion, decreasing the adiabatic losses and producing an enhancement of the radio luminosity due to particle re-acceleration and synchrotron losses, as also found in many young CSS sources (see e.g. Labiano et al. 2006; Oriente et al. 2007b). A similar result may be obtained when one jet has, for some reasons, an intrinsically higher internal pressure than the other. Another possible explanation is that component C consists of two components, i.e. the true core and a hotspot, as suggested by its resolved structure in the 15.3 GHz image. In this case J0951+3451 may be interpreted as an asymmetric source, where the core is closer to the brighter hotspot. On the other hand, component W, with its steep spectral index ( $\alpha \sim 1.0$ ) may represent a lobe-like feature where no particle acceleration is currently taking place.

In J1008+2533 the core component is the brightest one and it is located at its easternmost edge, from which a steep-spectrum jet emerges to the West. This source resembles the bright HFP quasar J2136+0041 (Oriente et al. 2006). Although both sources possess some amount of flux density variability, J2136+0041 preserves its convex spectral shape (e.g. Oriente et al. 2007b), whereas in J1008+2533 the radio spectrum during the last two observing epochs shows a flattening between 5 and 43 GHz, interpreted as the composition of two different spectra: convex below 8.4 GHz and inverted at higher frequencies (Oriente et al. 2010).

From this analysis we found that in five sources (J0905+3742, J0943+5113, J0951+3451, J1107+3421, and J1135+3524) the radio emission has a double/triple structure typical of young objects, while J1008+2533 displays a core-jet morphology, typical of blazars.

For the five sources marginally resolved at 15.3 GHz only, and for the six sources unresolved at both frequencies, the lack of information on the spectral index distribution does not allow us to classify their sub-components. However, if we consider the integrated spectral index we find that in two objects (J1241+3844 and J1319+4851) the spectrum turned out to be flat or inverted between 8.4 and 15.3 GHz, instead of steep as derived from the multi-epoch VLA campaign (Oriente et al. 2010). This strongly indicates the blazar nature of these two sources, and for this reason we drop these objects from the sample of genuinely young radio source candidates.

## 4.2 Flux density variability

In general, the flux densities measured in our VLBA images, and reported in Table 2, is a significant fraction, i.e. more than 80%, of those detected by VLA observations a few years earlier (Stanghellini et al. 2009; Oriente et al. 2010). This suggests that the majority of the observed sources (about 60%) are not significantly variable. In the remaining seven sources, the decreased flux densities detected by the VLBA with respect to those obtained from VLA observations may be related to some extended low-surface

brightness emission that cannot be accounted for due to the insufficient dynamic range of our observations. An example may be the radio galaxy J0943+5113, where diffuse emission connecting the main components is detected at 8.4 GHz, while it is resolved out at 15.3 GHz. In five sources (i.e. J0955+3335, J1002+5701, J1107+3421, J1436+4820, and J1613+4223) the flux density is continuously decreasing with time, when the VLA flux densities at the various epochs are compared. This behaviour may be explained by effective energy losses unbalanced by the acceleration of fresh particles, thus related to the evolution of a genuinely young radio source, rather than by variability related to boosting effects, like in blazars. However, in the case of J0955+3335 in addition to a decrease of the flux density, there is also a change in the spectral shape, which becomes much flatter,  $\alpha \sim 0.4$ , than in earlier VLA observations where the spectral index between 8.4 and 15.3 GHz was 0.7. Such a flattening, occurring in the optically-thin part of the spectrum, suggests that the variability in J0955+3335 is likely related to boosting effects as it happens in blazars. The sources J1008+2533 and J1319+4851 have similar VLBA and VLA flux densities at 8.4 GHz, while at 15.3 GHz our VLBA observations show a much higher flux density. This behaviour might be related to an increase of the core activity.

In summary, if we take into account all the pieces of information on the structure, spectral index and variability, we conclude that 6 objects (35%), labeled CSO? in Table 2, are to be considered CSO candidates, one object (6%) is a confirmed CSO, 4 objects (24%), labeled BL in Table 2, are part of the blazar population, while for the remaining 6 objects (35%) there is not enough information to reliably constrain the nature of their radio emission.

## 4.3 Physical properties

The knowledge of physical conditions in young radio sources is important for defining the framework of models describing radio source evolution. To draw a more comprehensive picture of the individual source evolution, we compare the physical parameters of these small and faint sources to those derived in other samples (both bright and faint) of HFP/GPS/CSS (e.g. Dallacasa et al. 2000; Fanti et al. 1990, 2001).

To adopt the same approach used in earlier works on CSS/GPS/HFP samples, we compute the physical parameters assuming that the sources are in the minimum energy condition, which corresponds to equipartition of energy between magnetic field and radiating particles (Pacholczyk 1970). Evidence in favour of this hypothesis has been found by Oriente & Dallacasa (2008b) by comparing the equipartition magnetic field with that computed on the basis of observed quantities like peak flux density, peak frequency, and linear size in self-absorbed components in a number of HFPs from the bright sample. In the present work we cannot perform such a computation since the two-frequency observations presented here are not adequate to estimate spectral peak values (frequency and flux density) for the individual components.

We computed the minimum energy density, minimum pressure and the equipartition magnetic field by means of the

standard formulae (Pacholczyk 1970), assuming equal energy between protons and electrons ( $k=1$ ), and an average optically-thin spectral index of 0.7.

The minimum energy density  $u_{\min}$  is derived from:

$$u_{\min} = 7 \times 10^{-24} \left(\frac{L}{V}\right)^{4/7} (1+k)^{4/7} \text{ erg cm}^{-3} \quad (1)$$

where  $L$  is the luminosity at 8.4 GHz in  $\text{W Hz}^{-1}$ , and  $V$  the volume in  $\text{kpc}^3$ , computed assuming an ellipsoidal geometry and a filling factor of unity (i.e. the source is fully and homogeneously filled with the relativistic plasma):

$$V = \frac{\pi}{6} d_{\min}^2 d_{\max} \quad (2)$$

where  $d_{\max}$  and  $d_{\min}$  are the component major and minor axes, in pc. The equipartition magnetic field is computed by:

$$H_{\text{eq}} = \sqrt{\frac{24}{7} \pi u_{\min}} \quad (3)$$

while the minimum pressure  $p_{\min}$  is  $\sim(1/3)u_{\min}$ .

From these equations we find that the typical values for the components of the faint HFP sample are:  $u_{\min} = 10^{-4} - 10^{-5} \text{ erg/cm}^3$ ,  $p_{\min} = 10^{-4} - 10^{-6} \text{ dyne/cm}^2$ , and  $H_{\text{eq}}$  ranges between 7 and  $\sim 60$  mG. Errors have been estimated by means of the propagation error theory and they are about 10% for  $H_{\text{eq}}$ . However, we must note that the uncertainties in the minimum energy parameters are strictly related to the assumptions of the value of both  $k$  and the filling factor, which may vary by several orders of magnitude.

The magnetic field values obtained are smaller than those usually found in the components of bright HFPs (Orienti et al. 2006), but they are in good agreement with those derived in the compact hotspots of CSS/GPS sources with similar luminosity (Dallacasa et al. 2002), while in the lobes of CSS/GPS sources such values are about 1-2 order of magnitude lower (e.g. Fanti et al. 1995). This result indicates that in the HFP sources the radio emission mainly comes from compact regions rather than from extended structures like lobes. In fact, the radiative lifetimes of relativistic electrons in such strong magnetic fields are very short and they are not expected to form a detectable back-flow lobe.

In Fig. 4, for the HFPs reported in Table 3 with a double/triple structure consistent with a young radio source, we show the magnetic field averaged over the whole source, obtained by considering the whole elliptical volume of the entire source, computed by means of Eq. 2, as filled by plasma (represented with X symbols in Fig. 4). As a comparison, the magnetic field computed in the same way for the sources from the bright HFP sample (Orienti et al. 2006) is shown as diamonds. This plot shows that the faint HFPs in this study have linear sizes comparable to those of the more compact bright HFPs but have magnetic fields like those in the most extended bright HFPs. The most compact (i.e. with sizes similar to those found in faint HFPs) and bright HFPs have instead larger fields. As expected, Fig. 4 shows that the higher magnetic fields are found in the most compact and brightest objects.

To investigate a possible evolution of the magnetic field as the source expands, we investigate its relation with the linear size  $r$  assuming pure adiabatic expansion. First of all, we as-

sume that the radio emission is due to a homogeneous component that is adiabatically expanding at a constant rate:

$$r = r_0 \left(\frac{t_0 + \Delta t}{t_0}\right) \quad (4)$$

where  $r_0$  is the source size at time  $t_0$  and  $r$  the size at the time  $t_0 + \Delta t$ .

We also assume that the magnetic field is frozen into the plasma:

$$H = H_0 \left(\frac{t_0}{t_0 + \Delta t}\right)^2 \quad (5)$$

where  $H_0$  is the magnetic field at the time  $t_0$  and  $H$  the magnetic field at the time  $t_0 + \Delta t$ .

To test the case of pure adiabatic expansion, we fit the magnetic fields and the linear sizes of the sources from the bright and faint sample separately, with the function:

$$H(t) = H_0 \left(\frac{r_0}{r_0 + r(t)}\right)^2 \quad (6)$$

where  $H_0$  and  $r_0$  are the magnetic field and size normalization, respectively, for the faint and bright samples separately. From Fig. 4 it is clear that the fit does not follow the expected magnetic field decrease as the source size increases, providing a reduced Chi-squared of 202 and 51 for the bright and faint sample, respectively. We must note that Eq. 6 represents a magnetic field that is frozen in a homogeneous component that is adiabatically expanding at a constant rate, without the injection/acceleration of new relativistic particles and no radiative losses. However, in young radio sources radiative losses play a major role given the high values of the magnetic field. Radiative losses would decrease the flux density mainly in the optically-thin part of the spectrum, thus underestimating the magnetic field. On the other hand, the injection/acceleration of relativistic particles is still taking place, as proved by the detection of the source core and hotspots. The continuous refueling of relativistic particles, and thus energy and magnetic field, implies that the initial conditions we considered for a frozen magnetic field are not suitable. Furthermore, the source is not likely evolving as a homogeneous component. Therefore, it is clear that the equipartition fields we determine as a function of the source size (i.e. the source age) need a more complex framework. The magnetic field can depend on the fate of individual components of each radio source. To study this aspect, in Fig. 5 we plot the equipartition magnetic field, computed following Eq. 3 and listed in Table 3, of all the components of each non-blazar object with resolved structure (i.e. at least two components per source) versus the source linear size. From this plot it is rather clear that the field intensities found in the various components of the same object can vary up to an order of magnitude. Such differences may arise from asymmetries in the source propagation, for example when the two sides experience a different environment.

All these pieces of evidence indicate that simple self-similar evolution models are not adequate to describe the radio source growth, as also pointed out by Sutherland & Bicknell (2007), Bicknell et al. (2003) and Fanti & Fanti (2003). To reproduce the evolution of the magnetic field, and thus of the radio source itself, a more complicated model taking

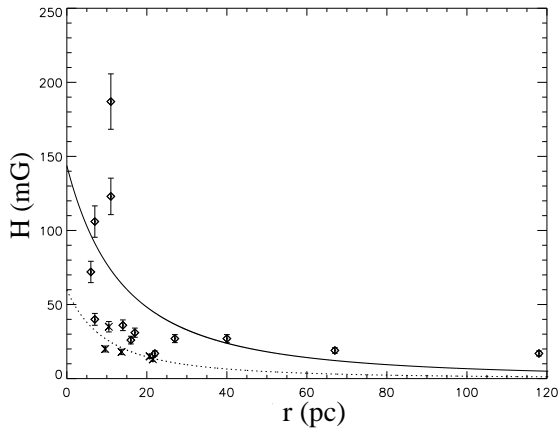


**Figure 4.** Equipartition magnetic field  $H$  versus the linear size  $r$  of the genuine CSOs from the faint ( $X$  symbols), and the bright (diamonds) samples. The lines represent the best fit to the model given in Equation 6 for the genuine CSOs and CSO candidates from the bright (solid line), and the faint (dotted line) sample, as described in Section 4.3.

into account the various physical and observational properties, as well as the ambient conditions must be considered.

## 5 SUMMARY

We presented VLBA observations at 8.4 and 15.3 GHz of 17 sources from the “faint” HFP sample (Stanghellini et al. 2009). The sources were selected on the basis of their peak frequency occurring below 8.4 GHz, in order to study their properties in the optically-thin part of the spectrum. We found that 11 objects are resolved into two/three components, while 6 are unresolved even at 15.3 GHz. When we complement the information on the structure with that on the spectral index distribution we found that in 7 of the resolved objects the radio emission is likely dominated by hotspots, as in genuine young radio sources, whereas 2 objects display a core-jet structure, typical of the blazar population. In the case of the unresolved sources, although nothing could be said on their structure, the availability of the two frequencies allowed us to find 2 sources whose spectra turned out to be flat/inverted between 8.4 and 15.3 GHz, indicating a change in the spectral index with respect to that derived from previous VLA observations (Oriente et al. 2010), and thereby implying strong variability in these sources. The component magnetic fields are similar to the values in the hotspots of young sources with larger sizes, but smaller than those found in the “bright” HFPs. Such high magnetic fields cause severe radiative losses, precluding the formation of extended lobe structures.

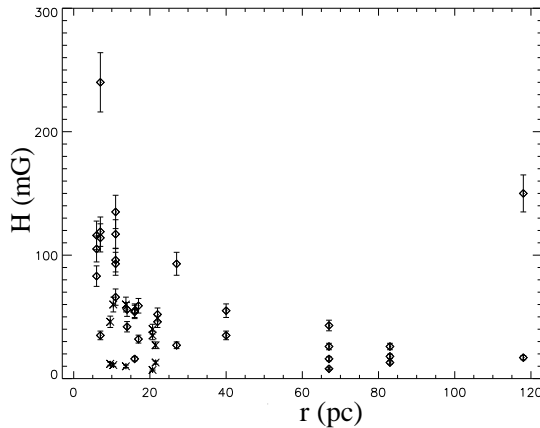


**Figure 5.** Single component equipartition magnetic field  $H$  versus the source linear size  $r$  of the components of the genuine CSOs and CSO candidates from the faint ( $X$  symbols), and the bright (diamonds) samples.

**Table 4.** Accurate position of the sources observed with the phase-referencing technique. The uncertainty on the source position is 0.5 mas (see Section 3).

Source	RA (J2000)	Dec (J2000)	Cal. source
J0736+4744	07:36:01.0496	47:44:23.991	J0742+4900
J0804+5431	08:04:59.2531	54:31:57.804	J0742+4900
J0943+5113	09:43:51.8174	51:13:22.537	J0929+5013
J1002+5701	10:02:41.6662	57:01:11.483	J0921+6215
J1107+3421	11:07:34.3384	34:21:18.596	J1130+3815
J1135+3624	11:35:52.2921	36:24:22.011	J1130+3815
J1241+3844	12:41:43.1334	38:44:04.271	J1242+3751
J1309+4047	13:09:41.5089	40:47:57.235	J1329+5009
J1319+4851	13:19:30.2948	48:51:03.194	J1329+5009
J1420+2704	14:20:51.4880	27:04:27.045	J1407+2827
J1436+4820	14:36:18.9097	48:20:41.135	J1407+2827

## ACKNOWLEDGMENTS

We thank the referee Jonathan Marr for carefully reading the manuscript. The VLBA is operated by the US National Radio Astronomy Observatory which is a facility of the National Science Foundation operated under cooperative agreement by Associated Universities, Inc. This work has made use of the NASA/IPAC Extragalactic Database NED which is operated by the JPL, Californian Institute of Technology, under contract with the National Aeronautics and Space Administration.

## REFERENCES

Becker, R.H., White, R.I., Helfand, D.J., 1995, ApJ, 450, 559

- Bicknell, G.V., Saxton, C.J., Sutherland, R.S., 2003, PASA, 20, 10
- Bolton, R.C., Chandler, C.J., Cotter, G., Pearson, T.J., Pooley, G.G., Readhead, A.C.S., Riley, J.M., Waldram, E.M., 2006, MNRAS, 370, 1556
- Dallacasa, D., Stanghellini, C., Centonza, M., Fanti, R., 2000, A&A, 363, 887
- Dallacasa, D., Tinti, S., Fanti, C., Fanti, R., Gregorini, L., Stanghellini, C., Vigotti, M., 2002, A&A, 389, 115
- Fanaroff, B.L., Riley, J.M., 1974, MNRAS, 167, 31
- Fanti, R., Fanti, C., Schilizzi, R.T., Spencer, R.E., Nan Rendong, Parma, P., van Breugel, W.J.M., Venturi, T., 1990, A&A, 231, 333
- Fanti, C., Fanti, R., Dallacasa, D., Schilizzi, R.T., Spencer, R.E., Stanghellini, C., 1995, A&A, 302, 31
- Fanti, C., Pozzi, F., Dallacasa, D., Fanti, R., Gregorini, L., Stanghellini, C., Vigotti, M., 2001, A&A, 369, 380
- Fanti, C., Fanti, R., 2003, ASPC, 300, 81
- Hancock, P.J., 2009, AN, 330, 180
- Hancock, P.J., Sadler, E.M., Mahony, E.K., Ricci, R., 2010, MNRAS, 408, 1187
- Labiano, A., Vermeulen, R.C., Barthel, P.D., O'Dea, C.P., Gallimore, J.F., Baum, S., de Vries, W., 2006, A&A, 447, 481
- Murgia, M., 2003, PASA, 20, 9
- O'Dea, C.P., Baum, S.A., 1997, AJ, 113, 148
- Orienti, M., Dallacasa, D., Fanti, C., Fanti, R., Tinti, S., Stanghellini, C., 2004, A&A, 426, 263
- Orienti, M., Dallacasa, D., Tinti, S., Stanghellini, C., 2006, A&A, 450, 959
- Orienti, M., Dallacasa, D., Stanghellini, C., 2007a, A&A, 461, 923
- Orienti, M., Dallacasa, D., Stanghellini, C., 2007b, A&A, 475, 813
- Orienti, M., Dallacasa, D., 2008a, A&A, 479, 409
- Orienti, M., Dallacasa, D., 2008b, A&A, 487, 885
- Orienti, M., Dallacasa, D., 2010, MNRAS, 406, 529
- Orienti, M., Dallacasa, D., Stanghellini, C., 2010, MNRAS, 408, 1075
- Owsianik, I., Conway, J.E., 1998, A&A, 337, 69
- Owsianik, I., Conway, J.E., Polatidis, A.G. 1998, A&A, 336, 37
- Pacholczyk, A.G., 1970, Radio Astrophysics (San Francisco: Freeman & Co.)
- Polatidis, A.G., Conway, J.E., 2003, PASA, 20, 69
- Snellen, I.A.G., Schilizzi, R.T., Miley, G.K., de Bruyn, A.G., Bremer, M.N., Röttgoring, H.J.A., 2000, MNRAS, 319, 445
- Stanghellini, C., O'Dea, C.P., Dallacasa, D., Cassaro, P., Baum, S.A., Fanti, R., Fanti, C., 2005, A&A, 443, 891
- Stanghellini, C., Dallacasa, D., Orienti, M., 2009, AN, 330, 223
- Sutherland, R.S., Bicknell, G.V., 2007, ApJS, 173, 37
- Taylor, G.B., Marr, J.M., Pearson, T.J., Readhead, A.C.S., 2000, ApJ, 541, 112
- Tinti, S., Dallacasa, D., de Zotti, G., Celotti, A., Stanghellini, C., 2005, A&A, 432, 31
- Tornainen, I., Tornikoski, M., Teräsraanta, H., Aller, M.F., Aller, H.D., 2005, A&A, 435, 839
- Tornainen, I., Tornikoski, M., Lähteenmäki, A., Aller, M.F., Aller, H.D., Mingaliev, M.G., 2007, A&A, 469, 451
- Tschager, W., Schilizzi, R.T., Röttgering, H.J.A., Snellen,

I.A.G., Miley, G.K., 2000, A&A, 360, 887